ELSEVIER

Experimental and numerical study of notched SHS made of different S355 steels

Håkon Johannessen [a], Oddvar Hestetræet Johannessen [a], Miguel Costas [a], Arild Holm Clausen [a,*], Johan Kolstø Sønstabø [b]

[a] Centre for Advanced Structural Analysis (CASA), Department of Structural Engineering, Norwegian University of Science and Technology (NTNU), NO-7491 Trondheim, Norway
[b] Multiconsult, NO-0213 Oslo, Norway

ARTICLE INFO

ABSTRACT

This study compares the mechanical behaviour of square hollow sections (SHS) made of three different types of S355: cold-formed, hot-rolled and offshore steel. A material model and failure criterion for each steel type were calibrated based on quasi-static uniaxial tensile tests. The failure criterion applies a recently proposed through-thickness damage regularisation model with the purpose of accurately describing the load-bearing capacity using shell elements. Experimental three-point bending tests were conducted at both quasi-static and dynamic conditions. Notches were used to trigger failure in the tests. The cold-formed steel exhibited the highest yield stress of the three steel types, while the offshore steel displayed better ductility than the other two. The numerical simulations showed that a shell element model of the SHS incorporating the regularisation scheme was able to describe the material behaviour and predict failure.

1. Introduction

Today, several types of S355 steels are available. They differ in material properties, such as ductility and fracture toughness, but also price. More ductile materials are typically more expensive, and the question arises as to whether it is cost-effective to use a more expensive steel or not. For some critical structures, like offshore installations, it may be necessary to demand great ductility from the material. There is also a choice between cold-formed and hot-rolled sections. Choosing the optimal steel type needed for a specific structure can have significant economic advantages.

A review of the available literature reveals several studies discussing the differences in material properties of cold-formed and hot-rolled steel. Gardner et al. [1] performed an experimental study comparing the differences between rectangular hollow sections made of hot-rolled and cold-formed steel. The results suggested that the corner regions of the cold-formed sections exhibited increased yield stress and ultimate strength, which were mainly attributed to cold working during production. Additionally, the cold-formed section had somewhat larger geometric imperfections than the hot-rolled section, which were mostly caused by through-thickness residual stresses in the cold-formed steel. Guo et al. [2] studied the compressive strength of thick-walled cold-formed sections in S235 steel by performing coupon tests of both the corner regions and flat surfaces of the sections. The results indicated an

increase in yield stress and a decrease in ductility in the corner regions. Quach and Young [3] studied the differences in material properties between cold-formed and hot-rolled elliptic hollow sections. The cold-formed section exhibited enhanced material strength, while the material properties of the hot-rolled section were relatively unchanged from the virgin material. The main differences in the material properties were caused by the reduction in residual stresses due to heat treatment of the hot-rolled section. Sun and Packer [4] investigated the differences in the static properties of cold-formed steel manufactured using three different methods: (1) direct-forming, (2) continuous-forming and (3) continuous-forming including stress-relieving heat treatment. Stress-strain behaviour and longitudinal residual stresses were compared in the different cold-formed steels. Results suggested that ultimate strengths were generally higher in the corner regions, and stress-relieving through heat treatment could also enhance the ductility of the cold-formed steel. In another study, Sun and Packer [5] presented a comprehensive investigation of the dynamic material properties of rectangular hollow sections made of cold-formed steel. They found that the dynamic increase factor, defined as the ratio between the yield stress at dynamic and quasi-static loading, was around 1.2 at strain rates of order 100 s^{-1}. Similar or slightly lower dynamic increase factors have been reported for hot-rolled steel [6–8]. The ductility at strain rates around 100 s^{-1} appears to be close to the ductility at quasi-static conditions.

Modelling tools such as finite elements can help to determine which S355 type is best suited for a specific structure. For large-scale modelling, shell elements are the reasonable choice compared to solid elements. When modelling with solid elements, a certain number of

elements over the thickness is needed in order to capture the stresses correctly. As a result, the computational expense is usually too high for industrial use and shell elements are preferred instead.

Sometimes the prediction of failure is of interest and damage and failure models may be incorporated in the numerical model. However, shell elements have limitations that make damage and failure modelling challenging. Firstly, shell elements cannot represent necking correctly because the elements are too large to capture the local deformations in the neck. In addition, failure modelling is a mesh dependent problem when using shells. During strain localisation, a fine discretisation would result in a higher local failure strain than a coarser discretisation. Additionally, during the evolution of the neck a triaxial stress state develops, which cannot be simulated accurately with shell elements due to the assumption of plane stress conditions in the element formulation.

As a remedy against the mesh-dependency when modelling ductile failure with shell elements, several size regularisation strategies have been suggested. Yamada et al. [9] performed numerical simulations of a buffer bow protection device for oil tankers by utilizing Barba's law to calculate fracture strains. In a paper investigating metal sheet forming by Hogström et al. [10], Barba's law was used in combination with forming limit curves. Forming limit tests were run and the results were implemented in numerical simulations with good results. Hogström et al. [10] also implemented the Bressan-Williams-Hill instability criterion, which is a combination of Bressan and Williams' [11] criterion and Hill's [12] criterion. This criterion enabled the calculation of local necking in both the first and second quadrants of the forming limit diagram. This method was previously proposed in a paper by Alsos et al. [13]. Kõrgesaar et al. [14] investigated the effects of different element sizes for large shell elements exposed to three different stress states. The method entailed averaging stresses and strains in a specific volume and extrapolating the values in order to represent large elements. The same authors also published a paper about ductile fracture in panels by applying a fracture criterion dependent on mesh size, stress state and damage-induced softening [15]. An alternative approach where a triaxiality-based failure criterion was combined with arbitrary forming limit diagrams was presented by Walters [16].

In the literature referenced above, regularisation schemes have been limited to membrane-dominated loading. During bending, metal sheets will show a greater ductility than in cases where membrane forces dominate. This is because the local necking that occurs under membrane loading is not present in bending, as the compressed side prevents the tension side from forming a neck [17]. The ductility of each shell element can be made dependent on the ratio between membrane and bending loading in order to describe ductility accurately. Costas et al. [18] proposed recently a failure model which takes both membrane and bending loading into account. This model incorporates a through-thickness damage regularisation scheme for shells (TTR) which computes failure as a function of the ratio between membrane and bending loading for each element.

The objective of this study is twofold. Firstly, to compare the mechanical behaviour of three different types of S355 square hollow sections by performing uniaxial tensile tests and calibrating material parameters. Secondly, to calibrate a failure model according to the TTR model proposed by Costas et al. [18], and attempt to validate the damage model for S355 notched hollow sections through quasi-static and dynamic three-point bending tests.

The following sections elaborate on the experimental testing, the numerical modelling and the calibration of the through-thickness damage regularisation model.

2. Material testing

2.1. Steel materials

In this study, square hollow sections (SHS) 120 × 120 × 5.0 mm (width × height × thickness) made of three different types of steel

Table 1
Survey of steel materials.

Notation	Steel designation	Standard
Cold-formed	S355J2H	NS-EN 10219-1 [21]
Hot-rolled	S355J2H	NS-EN 10210-1 [22]
Offshore	S355NH	NS-EN 10225-3 [23]

S355 were investigated. The SHS are herein denoted as cold-formed, hot-rolled and offshore steel, and were fabricated using different production routes according to European standards, presented in Table 1. All sections were delivered off-the-shelf by a wholesaler.

One of the most notable differences in how the SHS are produced occurs in the latter production stage. Here, the virgin material is formed into a circular cross section and welded, and subsequently shaped into the desired cross section. The hot-rolled and offshore SHS are formed at temperatures above 650 °C, which is the recrystallisation temperature of the steel. Additionally, the offshore SHS is normalized by re-heating above the A3-line in the iron-carbon phase diagram, and subsequently air-cooled. This results in a stress-relieved product with uniform mechanical properties. The last stage in the production process of the cold-formed SHS, on the other hand, is carried out at ambient temperature. As a consequence, significant cold working takes place during the forming of the SHS, especially in the corner regions. This results in through-thickness residual stresses building up in the cross-section, and also higher strengths and reduced ductility in the corners. In the hot-rolled and offshore SHS, these effects do not take place to the same degree. Therefore, as devised in the European standards, the corner radii in the cold-formed SHS are larger than those in the hot-rolled/offshore steel in order to prevent cracks during forming [19,20].

2.2. Material test set-up

Tensile tests were performed in order to characterise the mechanical behaviour of the materials. Specimens were extracted from the SHS made of the three steel materials addressed in Table 1. The nominal dimensions of the tensile test samples are available in Fig. 1. The specimens were collected from different walls of the profiles to obtain representative results. The material properties in the areas around the welds and the corners may differ from the rest of the SHS [4]. Applying a modelling strategy suitable for industrial purposes, the material calibration was simplified by extracting samples neither close to the corners nor close to the welds. It is worth noting that the cold-formed specimens obtained from the longitudinal direction were slightly bent after extraction from the SHS. This was most likely caused by through-thickness bending residual stresses induced in the forming process of the hollow section [24]. This curvature is assumed to have negligible influence on the test results in the plastic domain because the specimens straightened out during the beginning of the tensile tests.

The test specimens were sampled both parallel (0°) and transverse (90°) to the rolling direction in order to determine to what extent the material was isotropic. Additionally, some tensile tests were performed at an increased strain rate to explore rate-dependent behaviour. The lower strain rate of 10^{-3} s^{-1} corresponds to a quasi-static loading condition, while a two-decade increase to 10^{-1} s^{-1} is sufficient to disclose
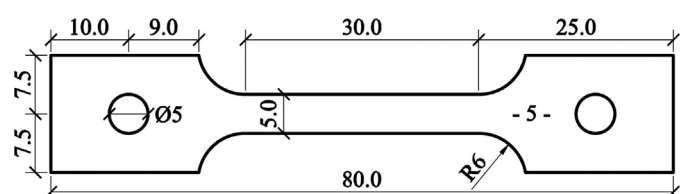

Fig. 1. Tensile test specimen with dimensions in mm.

Table 2
Tensile test matrix of the steel materials indicating the number of replicates of each test.

Steel material		Offshore		Hot-rolled		Cold-formed	
Loading rate	Nominal strain rate	0°	90°	0°	90°	0°	90°
1.8 mm/min	10^{-3} s^{-1}	3	3	3	3	3	2
180 mm/min	10^{-1} s^{-1}	3	0	3	0	2	0

whether a strain-rate effect is present. It was feasible to obtain a strain rate of 10^{-1} s^{-1} without any disturbance of the recorded data due to inertia effects of the test machine. The test matrix is available in Table 2, where the figures indicate the number of replicates run for each case. A total of 25 uniaxial tensile tests were performed.

Two Basler acA4112-8gc cameras monitoring one in-plane and one out-of-plane surface of the specimen shown in Fig. 1 were set up to capture the deformation during the tensile tests. The acquisition frequency of the cameras was 1 Hz. The force and displacement data from the actuator were captured by the load cell in the test machine and was used as a cross-check of the displacement obtained by the cameras. Prior to each test, the thickness and width of the test specimens were measured with a sliding caliper at three different points in the gauge area. All samples were sprayed with a black and white speckle pattern, which was necessary for digital image correlation (DIC) analysis. Applying DIC, the strain field on the surface of the gauge area could be measured until failure. The in-house DIC software eCorr [25,26] was used for the DIC analysis. Fig. 2 shows pictures of a tensile specimen before and after testing and a photo of the test setup.

2.3. Results from material tests

Engineering strains were obtained by digital image correlation, placing a virtual extensometer with an initial length of 15 mm on the

pictures of the test specimens. The engineering stress-strain curves from the 25 tests are provided in Fig. 3. Weak anisotropy is observed for all three steel types. The most notable difference between the transverse and longitudinal specimens is a slightly lower ductility in the transverse direction, while both the work-hardening and ultimate strength are relatively similar. One representative curve obtained at 10^{-3} s^{-1} in the 0° -direction for each steel material is displayed in Fig. 3d.

The proof stress of the cold-formed steel was determined to be 460 MPa, while the yield stress for the hot-rolled steel and the offshore steel was 390 MPa and 428 MPa, respectively. Furthermore, the ultimate engineering stress was 552 MPa for the cold-formed steel, 542 MPa for the hot-rolled steel and 542 MPa for the offshore steel. These values are significantly higher than the minimum values provided in the the European standards [27]. In Eurocode 3, the characteristic yield stress for all three steel types is 355 MPa, and the ultimate stress for cold-formed and hot-rolled steel is 510 MPa and for the offshore steel it is 490 MPa. It is worth noting that the results of the offshore steel had a larger scatter than the two other steel types. The cold-formed steel separates itself from the other types by not having a yield plateau. This is a consequence of the work-hardening experienced during the production routine. The work-hardening also caused an increased initial yield stress in the cold-formed steel.

Fig. 3a to c also display the additional tensile tests performed at an elevated strain rate of 10^{-1} s^{-1}. All the steel types exhibited an increase in ultimate stress. Slightly depending on the material, the increase was approximately 40 MPa, and the corresponding dynamic increase factor, calculated as the ratio of the ultimate stress at 10^{-1} s^{-1} and 10^{-3} s^{-1}, was around 1.1. This agrees fairly well with a factor of 1.2 at strain rate 10^2 s^{-1} [5]. Moreover, it appears from Fig. 3a that the cold-formed steel was slightly less ductile at 10^{-1} s^{-1} than in the quasi-static tests. These observations indicate that the three materials are strain-rate sensitive.

(a)
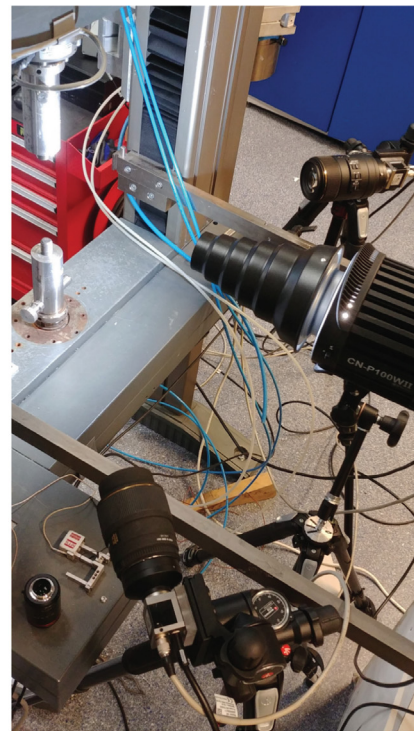
(b)

Fig. 2. Tensile specimen before and after test (a) and test setup for the material tests including two cameras and a lighting source (b).

(a) Cold-formed steel

(b) Hot-rolled steel

(c) Offshore steel

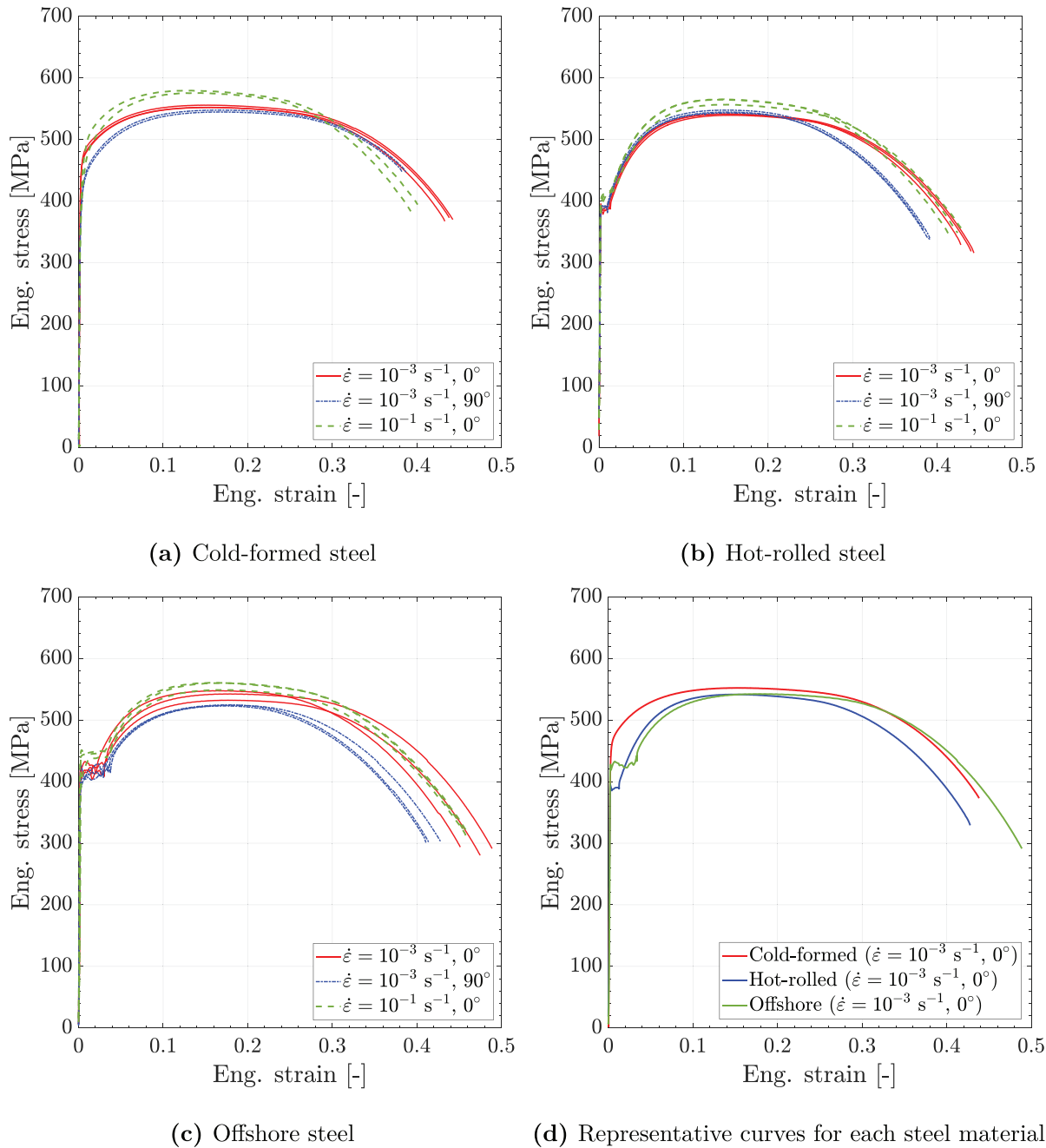(d) Representative curves for each steel material.

Fig. 3. Engineering stress-strain curves from all tests on the three steel types (a)(b)(c), as well as a comparison of representative tests (d).

3. Numerical model

A numerical model of the tensile specimen is required for calibration of the material model. The three symmetry planes were employed when modelling the specimen, see Fig. 4. Eight-node solid elements with a size of approximately 0.5 mm were applied in these simulations, resulting in a total of 10 elements over the thickness.

3.1. Material model

As mentioned previously in Section 2.2, weak anisotropy was observed in the three steel types. Yet, an isotropic material model was chosen for the numerical model because of its simplicity. In
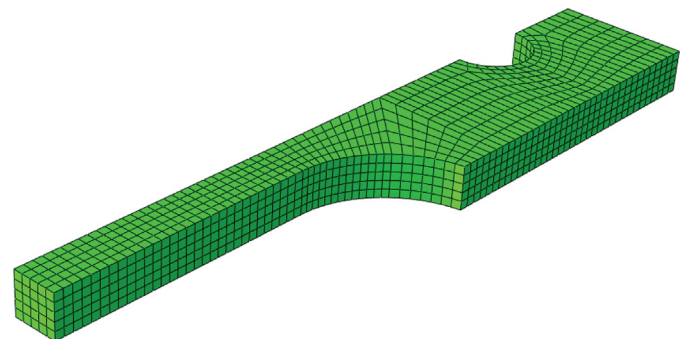

Fig. 4. Numerical model of 1/8 of the tensile specimen.

particular, calibrating an anisotropic model is more challenging, requires more testing and the computation time would increase significantly, making it less suitable for large-scale industrial applications.

Hence, an isotropic elastic-plastic material model with isotropic work-hardening was employed in the simulations. Young's modulus was assumed 210 GPa and the Poisson's ratio was set to 0.3, as customary. The yield function f is defined as

$$f(\sigma_{eq}, R) = \sigma_{eq} - (\sigma_0 + R) \leq 0 \tag{1}$$

where σ_{eq} is the equivalent stress, σ_0 is the yield stress of the material and R is the isotropic hardening variable. The von Mises yield criterion for isotropic plasticity was employed, reading

$$\sigma_{eq} = \left\{ \frac{1}{2} \left[(\sigma_1 - \sigma_2)^2 + (\sigma_2 - \sigma_3)^2 + (\sigma_3 - \sigma_1)^2 \right] \right\}^{\frac{1}{2}} \tag{2}$$

where σ_1, σ_2 and σ_3 are the ordered principal stresses. An extended Voce hardening law with three terms was used to express the work-hardening variable R, viz.

$$R(p) = \sum_{i=1}^{3} Q_i \left[1 - \exp\left(-\frac{\theta_i}{Q_i} p \right) \right] \tag{3}$$

where (Q_i, θ_i) are the work-hardening parameters and p is the equivalent plastic strain. The yield stress and work-hardening parameters were determined using an inverse modelling approach with the
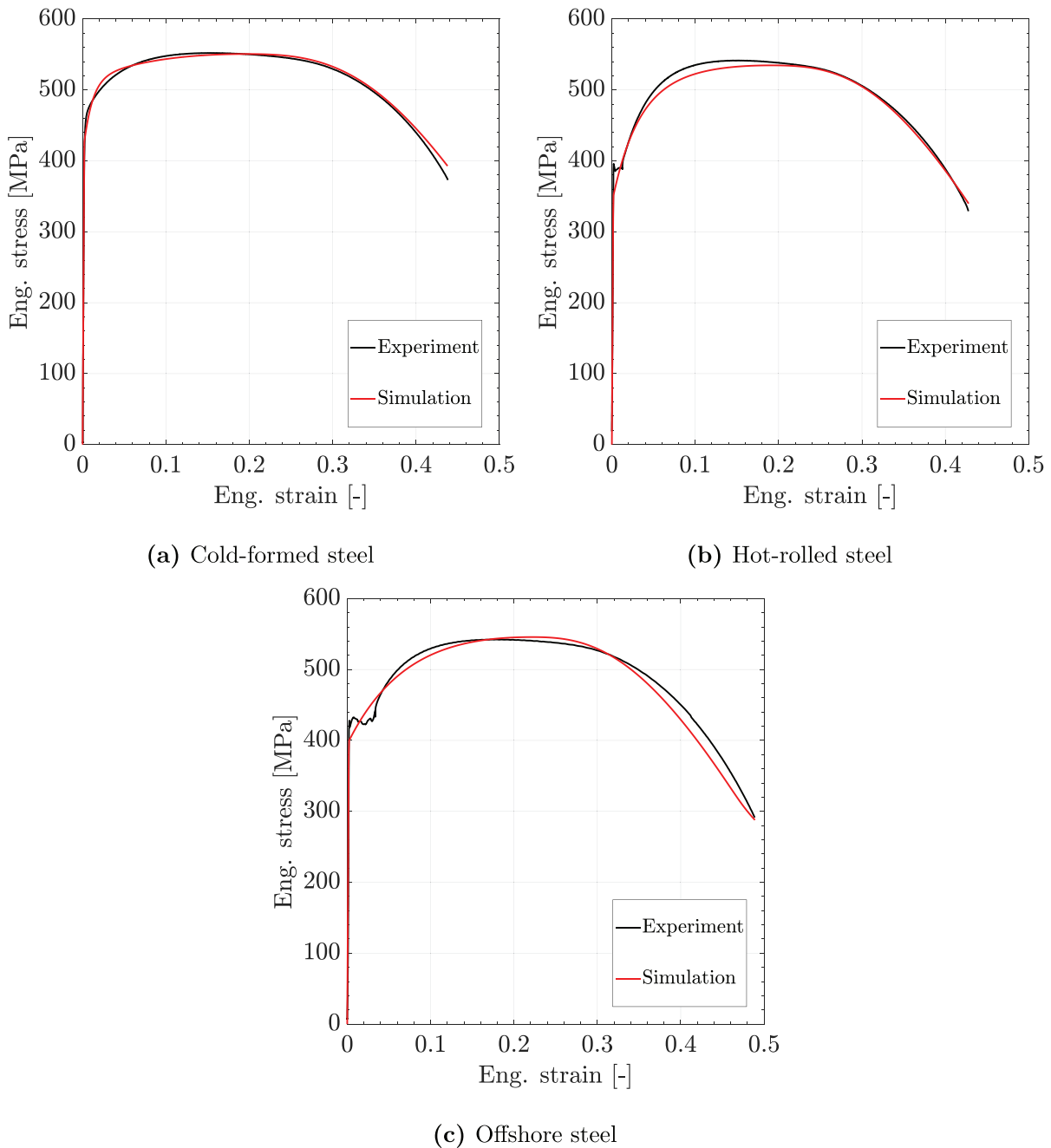

(a) Cold-formed steel

(b) Hot-rolled steel

(c) Offshore steel

Fig. 5. Numerical engineering stress-strain curves based on the material calibrations of the three steel types using the extended Voce hardening law.

Table 3
Yield stress and work-hardening parameters of the three steel materials, given in MPa.

Steel type	σ_0	Q_1	θ_1	Q_2	θ_2	Q_3	θ_3
Cold-formed	426.9	87.71	8804	210.4	665.8	296.6	333.6
Hot-rolled	350.3	85.79	3076	337.0	1065	59.08	1843
Offshore	399.6	117.8	1701	171.4	682.3	176.3	388.7

Table 4
Failure parameters for the three steel materials.

Steel types	W_C^b [MPa]	W_C^s [MPa]	W_C^l [MPa]	c
Cold-formed	861.1	276.0	139.1	0.84
Hot-rolled	719.7	328.8	175.7	1.10
Offshore	1076	315.6	176.6	1.44

optimization tool LS-OPT [28]. With this method, the engineering stress-strain curves obtained from Abaqus/Standard [29] simulations were optimized to fit the representative engineering stress-strain curves shown in Fig. 3d. The fitted curves for each steel type are reported in Fig. 5 and the material parameters are available in Table 3.

The Voce hardening law cannot describe the yield plateau exhibited by the hot-rolled and offshore steels. Because the sizes of the yield plateaus were small compared to the total plastic strain at failure, it was deemed acceptable to ignore them in the calibration of the work-hardening laws. This resulted in lower yield stresses and steeper work-hardening in the early plastic domain, see Fig. 5b and c.

3.2. Through-thickness damage regularisation scheme

In the through-thickness damage regularisation scheme proposed by Costas et al. [18], the Cockcroft-Latham [30] fracture criterion was adopted. The damage variable was defined as

$$D = \frac{1}{W_C} \int_{p=0}^{p=p_f} \max\{\sigma_1, 0\} \; \mathrm{d}p \tag{4}$$

where D is the damage variable, W_C is an experimentally determined fracture parameter, p_f is the equivalent plastic strain at failure, σ_1 is the major principal stress and p is the equivalent plastic strain. Shell elements are not able to capture necking accurately. Thus, artificial reduction of the elements' ductility is required, but this reduction is dependent on whether the loading mode is dominated by membrane forces or bending. As a result, two Cockcroft-Latham parameters are needed, W_C^m and W_C^b, where the superindices indicate membrane and bending governed failure, respectively. The local fracture parameter W_C is calculated from:

$$W_C = \Omega W_C^b + (1-\Omega) W_C^m \tag{5}$$

where Ω is the deformation mode indicator. The purpose of Ω is to balance the amount of bending and membrane loading in each element. It is defined as:

$$\Omega = \frac{1}{2} \frac{|\varepsilon_{p,33}^T - \varepsilon_{p,33}^B|}{\max\left\{|\varepsilon_{p,33}^T|, |\varepsilon_{p,33}^B|\right\}} \tag{6}$$

where $\varepsilon_{p,33}^T$ and $\varepsilon_{p,33}^B$ are the through-thickness plastic strains at the integration point on the top and bottom of each element, respectively. The deformation mode indicator will have a value of 1 under pure bending and a value of 0 under pure membrane loading.

The two Cockcroft-Latham parameters for membrane dominated and bending dominated loading were calibrated separately. The membrane parameter W_C^m can be described by the following exponential decay expression [31]:

$$W_C^m = W_C^l + \left(W_C^s - W_C^l\right)e^{(-c(l_e/t_e - 1))} \tag{7}$$

where W_C^l, W_C^s and c are experimentally determined parameters and l_e/t_e is the element's length-to-thickness ratio, or aspect ratio. To calibrate the parameters, vectors with different lengths l_e, tracking longitudinal elongations, were placed in the necking region of the DIC images. The elongations were applied as boundary conditions to single shell element models with aspect ratios matching the vector lengths. As a result, the element was loaded in uniaxial tension until the elongation of the element corresponded to the elongation of the DIC vector at failure, and the Cockcroft-Latham parameter for membrane governed failure was calculated by numerical integration. The results were fitted to Eq. (7) and the parameters are reported in Table 4.

The Cockcroft-Latham parameter for bending governed failure, W_C^b, determines the onset of failure without strain localisation. The parameter was obtained by running fine-meshed solid simulations of the tensile tests in Abaqus/Standard. This was performed in the same manner as detailed by [18]. The bending parameters for the three steel types are available in Table 4.

4. Quasi-static three-point bending tests

4.1. Experimental study

A series of quasi-static three-point bending tests were conducted in an effort to validate the material models and to investigate the mechanical behaviour of the three steel materials. The components were 600 mm long $120 \times 120 \times 5.0$ mm SHS of the three steel types presented in Section 2.1. Each component had a 50 mm notch placed 60 mm off-center with the purpose of provoking failure, see Fig. 6. The offset of the notch was intended to provoke a diagonally propagating crack, which is an additional challenge for the finite element simulations with shell elements. The diameter of the notch was chosen in a way such that it could accommodate a certain number of elements in the simulations, even with coarse discretisations.

The tests were performed using an Instron testing rig mounted with a 500 kN load cell. The actuator was equipped with a cylinder with a diameter of 60 mm that was in contact with the specimen, and moved at a constant velocity of 10 mm/min. To minimise friction, polytetrafluorethylen (PTFE) sheets of 3 mm were placed at the supports and actuator, see Fig. 7. The supports were also cylindrical with diameter 60 mm. Three repetitions were run for each steel type.

Three cameras were set up to record the three-point bending tests. Two Prosilica GC2450 5.0 MP cameras captured the deflection of the beams globally and locally around the notch. The cameras were
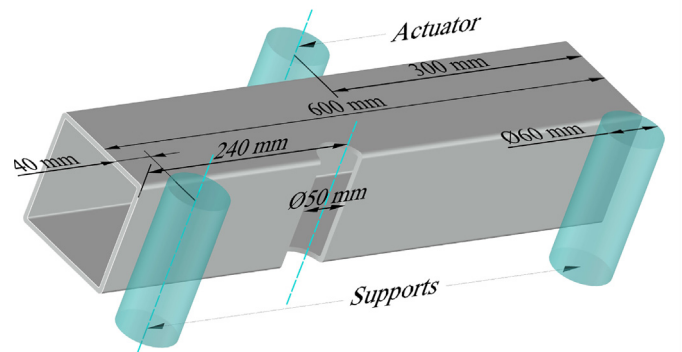

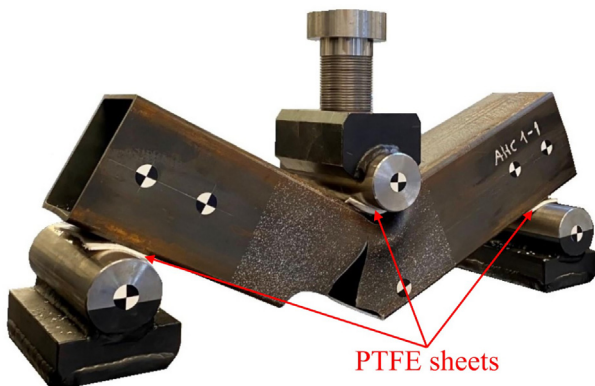**Fig. 6.** Dimensions of the three-point bending test specimens.

Fig. 7. Three-point bending test set-up.

Fig. 9. Finite element model of the quasi-static three point bending.

mounted 170 cm and 139 cm from the beam, respectively. At the opposite side of the beam, a Basler acA4112-8gc 12.3 MP camera was mounted 128 cm from the beam and captured the center area of the rear side of the beam. A speckle of black and white paint was added in the central area on both sides of the beam, see Fig. 8a, facilitating for DIC analysis. Moreover, stickers were placed in convenient positions to determine the horizontal and vertical displacement components accurately at these locations with use of pictures from the global camera, see Fig. 7.

The load cell mounted on the test machine measured the force during the experiments. Additionally, the displacements were determined by running point tracking on the sticker at the actuator with eCorr. It was observed that the PTFE sheets were compressed during the initial loading, slightly lowering the beam. This in turn influenced the gradient of the force-displacement curve in the elastic area, resulting in an overly-soft slope. In order to correct this, the vertical deflection of the two stickers located directly above the supports were tracked and the average deflection in the elastic phase of these two stickers were subsequently subtracted from the measured displacement in the actuator. The rest of the force-displacement data was shifted accordingly. This resulted in a steeper slope in the elastic area, without influencing the accuracy of the data. One of the offshore tests lacked a PTFE sheet on the actuator. This test had a steeper slope than the other two tests, even after corrections, see Fig. 10a to c.

A sudden drop in force occurred around 37 mm displacement for the cold-formed beams, see Fig. 10a. This was caused by ductile cracks at the transition zone between the corners and the top flange, see Fig. 8b. As mentioned previously, the corners of the cold-formed steel experienced work-hardening during production which increased their strength and reduced their ductility. This probably explains why only the cold-formed SHS experienced these cracks. The deformation mode of the cold-formed beam changed as a consequence, making the beam fail at a later displacement.

An additional observation was made in all post-mortem test specimens on how the fracture propagated during the test. The fracture
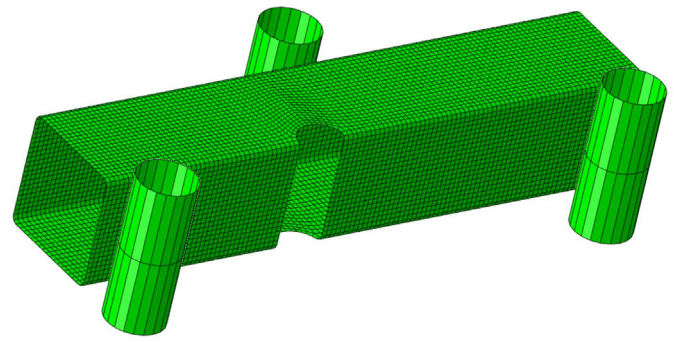
started in the upper part of the notch and propagated towards the contact point of the actuator. Fig. 8a shows how the fracture appeared in one of the post-mortem cold-formed test specimens.

4.2. Numerical study

The components were modelled in Abaqus/Explicit with four-node shell elements, see Fig. 9. Reduced integration, hourglass control and five through-thickness integration points were employed. The material model and damage regularisation strategy were implemented through a VUMAT user-defined subroutine in Abaqus. The average measured thickness of each hollow section was adopted in the numerical simulations. These thicknesses were: 4.79 mm for the cold-formed steel, 4.75 mm for the hot-rolled steel and 5.02 mm for the offshore steel. The four walls were given the same shell thickness.

Despite their reduced slenderness, the experimental components made of the three different steel types might have presented some geometrical imperfections that, in turn, could have affected their collapse modes. In order to assess whether these imperfections could be relevant in the current investigation, the geometrical tolerances provided in the standards [19–21] were applied to the finite element models by computing the most relevant eigenmodes of the components and applying the scaled modal displacements as initial imperfections, matching the maximum geometrical deviations stated in the standards. It was observed that the average forces obtained from the models with imperfections differed from those without imperfections by less than 2% in the worst case, and that the collapse modes were identical. Given these marginal differences, it was deemed acceptable to run the current component analyses without considering initial geometrical imperfections.

The profiles were quite thick, which limited the size of the elements that could be used in the simulations. A mesh size corresponding to an element length-to-thickness ratio of 1 was chosen for the different steel types. The PTFE sheets were not included in the model, but a low friction coefficient of 0.05 was employed. It was deemed reasonable to model the supports and the actuator as rigid surfaces. A time scaling
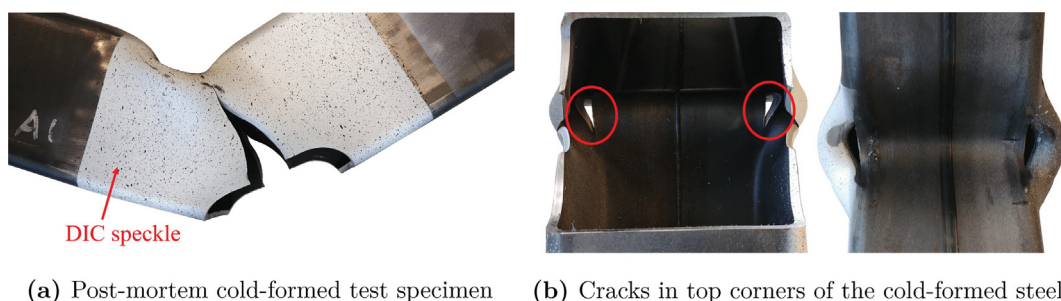

(a) Post-mortem cold-formed test specimen

(b) Cracks in top corners of the cold-formed steel.

Fig. 8. Cracks observed in the quasi-static test specimens.
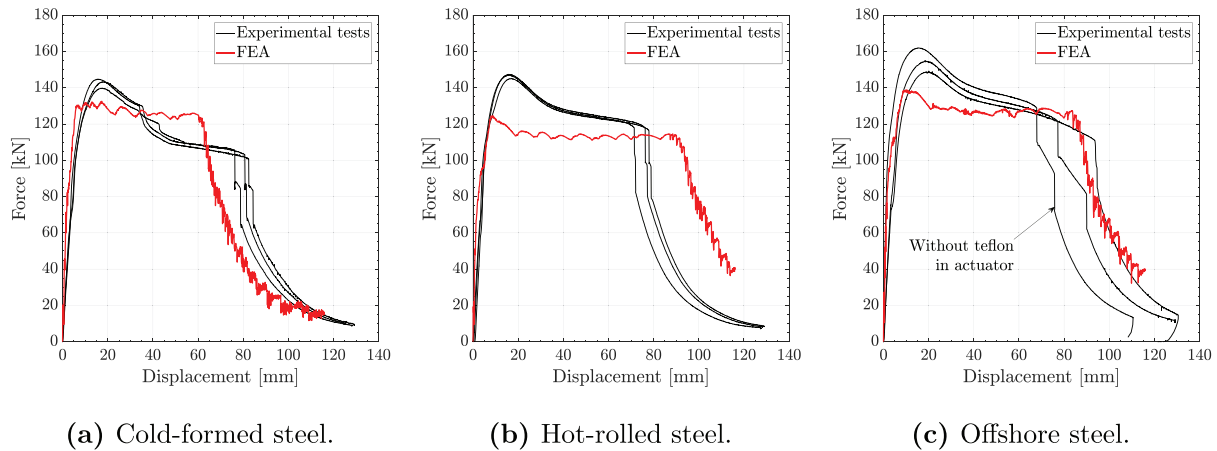
Fig. 10. Force-displacement curves from quasi-static tests and simulations on three-point bending tests, after PTFE corrections.

factor of 3000 was incorporated as a measure to reduce the computation time. The velocity of the actuator was, over the first tenth of the total step time, smoothly ramped up in order to ensure quasi-static conditions. The energy balance was checked after the simulations to confirm negligible inertial effects.

The force-displacement curves from the numerical simulations and experiments are compared in Fig. 10a to c for the three steel materials, respectively. The peak force of the cold-formed steel material, see Fig. 10a, is slightly underestimated. However, the main discrepancy is that the numerical analysis, where the material is assumed to be homogeneous, is not able to represent the reduced ductility close to the corners and the formation of local cracks, see Fig. 8b. Consequently, the drop in force around 37 mm displacement is not captured in the model.

The hot-rolled steel beams exhibited lower peak force and greater ductility in the numerical simulations compared to the experimental results. It seems reasonable to argue that the loss of absorbed energy at the peak force is compensated for by an increase of ductility in the simulations. The behaviour of the offshore steel was quite similar to that of the hot-rolled steel. The peak force was underestimated and the displacement at failure was overshot in the numerical simulation, except for one test. However, as pointed out in Section 2.2, the scatter in the material tests on the offshore steel material was notably larger than in the two other steel types. It is possible that the missing PTFE sheet on one of the offshore tests might explain the increased peak force for that particular specimen.

When studying the damage variable in the five section points of the shell elements, close to where the cracks occurred, only the top section points reached values close to 1. As a result, the elements did not erode, because the adopted failure model deletes elements only when the damage variable in their mid section point reaches a value of 1. Contour plots of the damage variable in the top section point are shown in Fig. 11a to c, while Fig. 11d to f display the top flange of one of each steel material post-mortem. It is visible from the plot of the cold-formed and the hot-rolled steel that some of the elements are close to reaching a value of one in the top section point. All the simulations with shells underestimated the peak force. When performing simulations with solids, the peak force was better captured. The numerical simulations using solids were not included in this paper due to brevity.

Contour plots from Abaqus of the damage variable D and the deformation mode indicator Ω are available in Fig. 12. Fig. 12d to f show the locations of where the damage was caused by membrane or bending dominated loads, or if it was caused by a combination of both. As seen, the mode indicator variable changes according to the deformation mode, being closer to zero in the notch and closer to one near the plastic hinge. The crack propagation follows the direction of the mesh rather than the straight line towards the actuator observed in the tests, Fig. 8a. This is usually the case when shell elements are used.

5. Dynamic three-point bending tests

5.1. Experimental set-up in the kicking machine

In addition to the quasi-static tests, a series of dynamic three-point bending tests were performed. The purpose of the dynamic tests was partly to explore any possible difference in the response of the beams in quasi-static and dynamic loading conditions, and partly to evaluate the performance of the TTR failure model in a dynamic case. The tests were performed using an in-house pendulum accelerator known as the "kicking machine". A detailed description of this test rig is provided in Hanssen et al. [32]. The machine has successfully been used to test a wide range of components, including, but not limited to, offshore pipelines [33], stiffened steel plates [34], crash boxes [35] and structural joints [36]. An illustration of the kicking machine set-up is shown in Fig. 13a. The test specimens were mounted vertically to the reaction wall, see Fig. 13b, by two elastic straps. The diameter of the cylinders at the supports and actuator was 50 mm. The hydraulically-driven rotating arm accelerated a trolley with a mass of 1470.7 kg to a prescribed velocity of 4.1 m/s. A load cell with a capacity of 500 kN was mounted at the front of the trolley. The impact was filmed by two Phantom v2511 high-speed cameras. All test specimens were sprayed on the impact area with a Kluber Unimoly C220 lubricant spray to reduce friction. The average thickness of the SHS applied in the dynamic tests were measured as 4.74 mm for the cold-formed steel, 4.70 mm for the hot-rolled steel and 4.98 mm for the offshore steel. Three repetitions of the impact test were performed for each steel type.

Oscillations were present in the test data from the dynamic tests and can be viewed in Fig. 14a. The oscillations are primarily attributed to impulse during the impact, which subsequently generated stress waves travelling back and forth in the load cell and trolley. This phenomenon is further described by Sønstabø et al. [36]. Additionally, the oscillations could be caused by vibrations in the test specimen during the impact. It was deemed reasonable to use a mathematical filter to remove the oscillations from the test results. A Savitzky-Golay filter with a window length of 1001 and polynomial order of three was applied to the test results. The effect of the applied filter is depicted for one of the hot-rolled tests in Fig. 14a. A laser measuring the displacement of the trolley and DIC tracking based on the camera footage were used as a cross-check of the accuracy of the load cell data. The different measurements of the displacements matched well, and the DIC-measurements were used in the forthcoming force-displacement curves. The small deflections in the supports which occurred during impact were tracked and
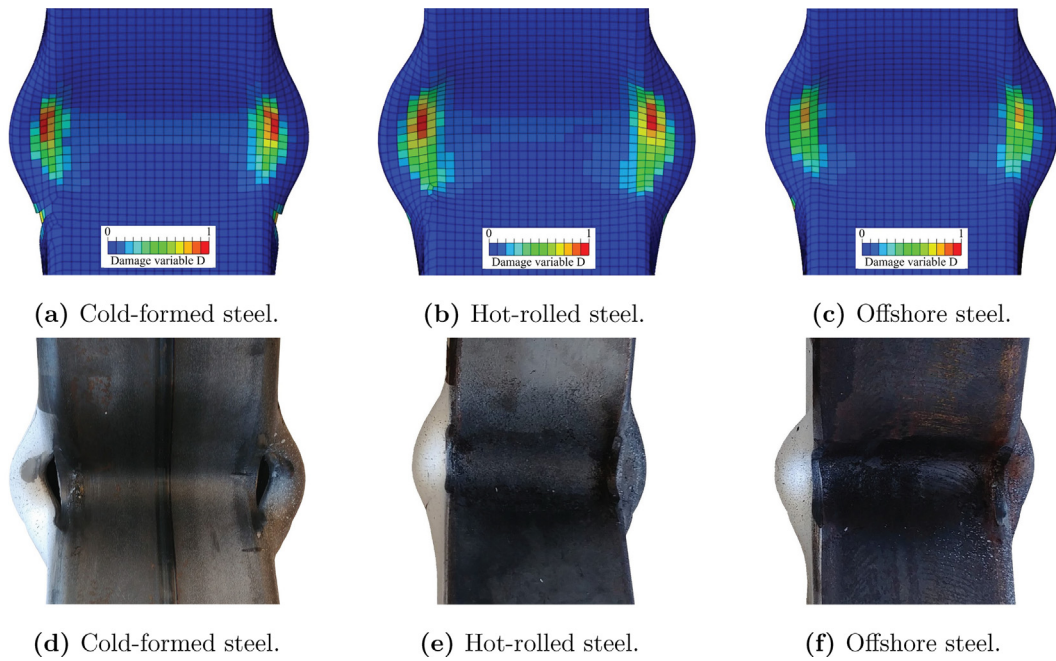
Fig. 11. Deformation mode in top flange of all three steel types. Figures (a)–(c) display contour plots of the damage variable D in top section point. Figures (d)–(f) show the top flange of the post-mortem quasi-static test specimens.
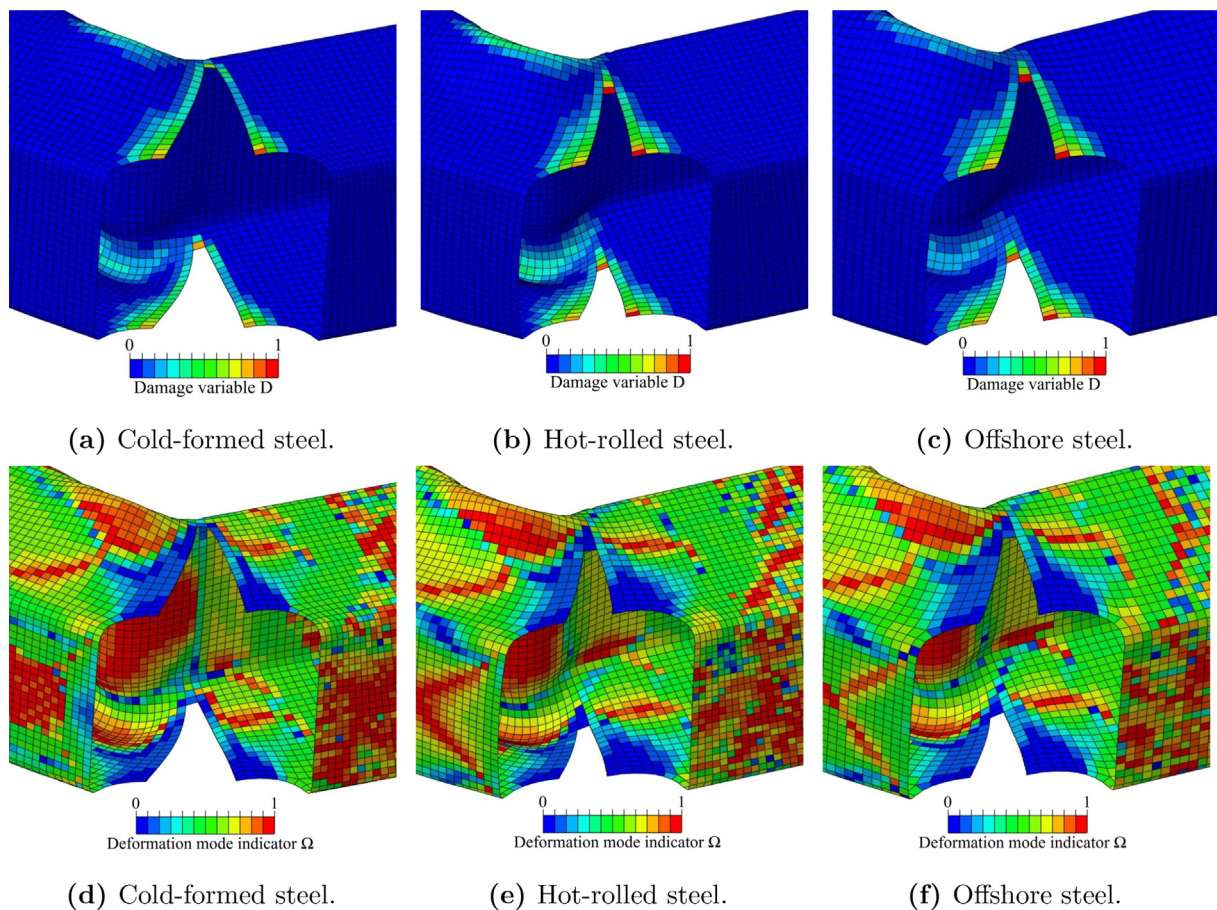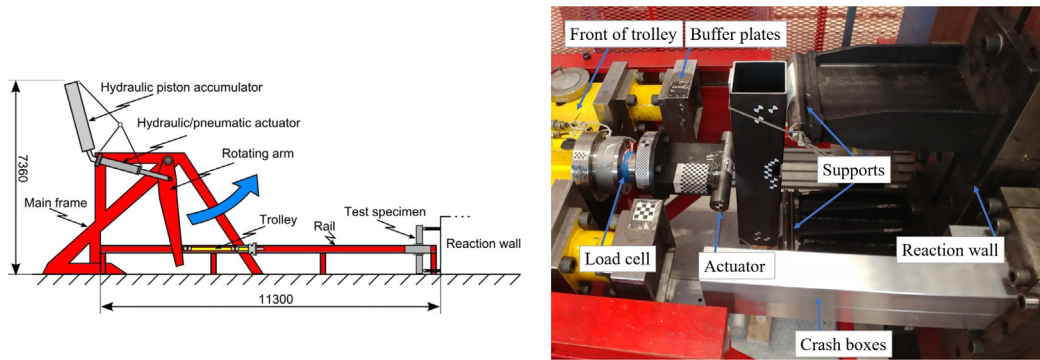

Fig. 12. Contour plots from simulations of the three steel types. Figures (a)–(c) provide the damage variable D and Figures (d)–(f) show the deformation mode indicator Ω. Pure membrane when $\Omega = 0$ and $\Omega = 1$ signify pure bending.

(a) Schematic diagram of the kicking machine, described by Grimsmo et al. [37].

(b) Set-up details.

Fig. 13. Set-up of dynamic tests in the kicking machine.

subsequently subtracted. Grimsmo et al. [37] provided further description of the different measuring techniques.

The quasi-static and dynamic test results are plotted side-by-side in Fig. 14b and c. The repeatability of both types of tests was good. It is apparent that all steel sections displayed rate-dependency, as the peak forces are higher and the displacements at failure were subsequently lower in the dynamic tests than in the quasi-static tests. Inertia effects could also contribute to the higher peak forces. The cold-formed

post-mortem specimens had similar cracks in the transition zone between the top corners and the top flange as were observed in the quasi-static tests, see Fig. 15a. Additionally, two of the hot-rolled specimens showed cracks in the top flange similar to those in the cold-formed steel, see Fig. 15b. However, this fracture only occurred in the welded corner on the top side of the specimens. In the third hot-rolled specimen, the weld was located in one of the bottom corners and post-mortem analysis showed no cracks there.

(a) Before and after filtering.

(b) Quasi-static test results.

(c) Dynamic test results.

(d) Dynamic cold-formed.
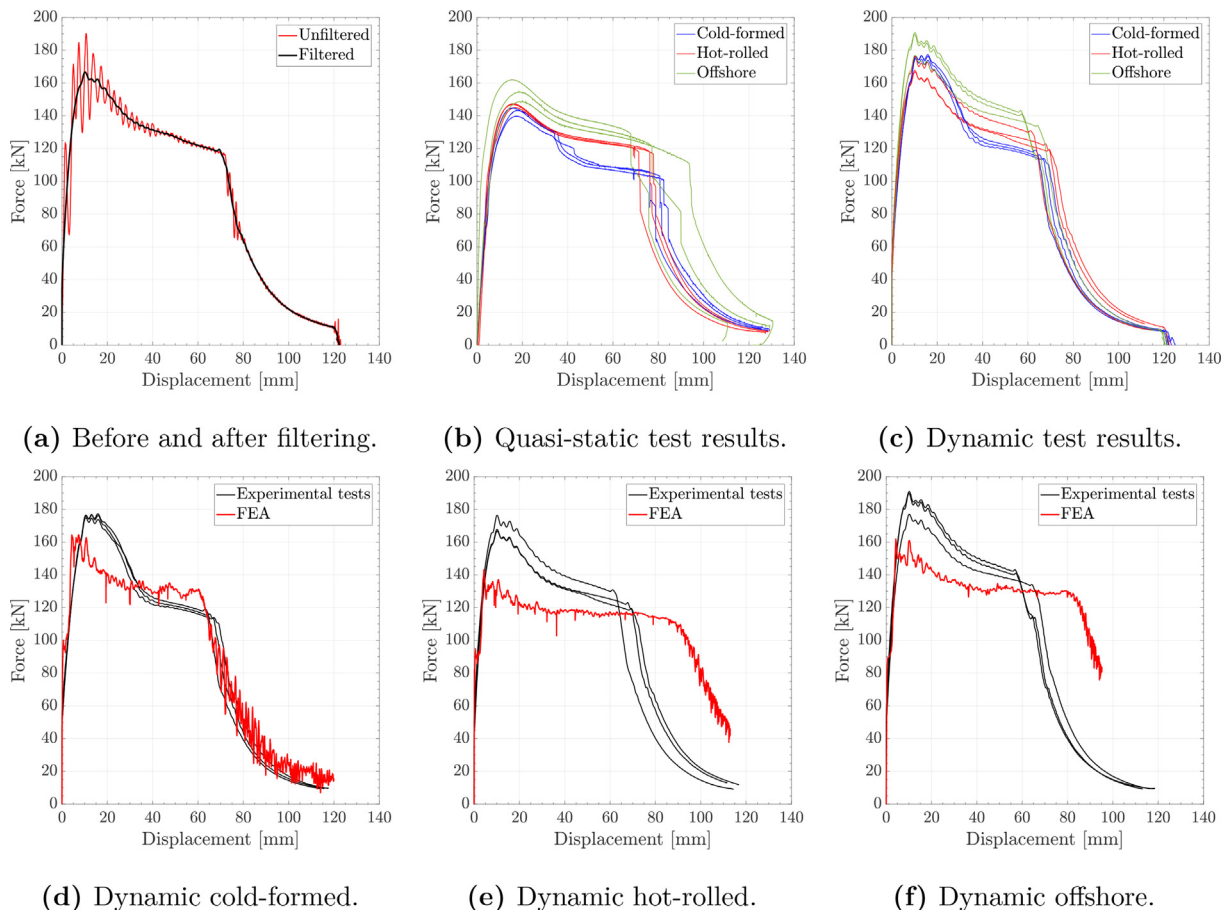
(e) Dynamic hot-rolled.

(f) Dynamic offshore.

Fig. 14. Pre and post-filtering on one test (a). Force-displacement curves of the quasi-static tests (b) and the dynamic test (c). Filtered force-displacement curves from the dynamic tests (d) (e) (f).
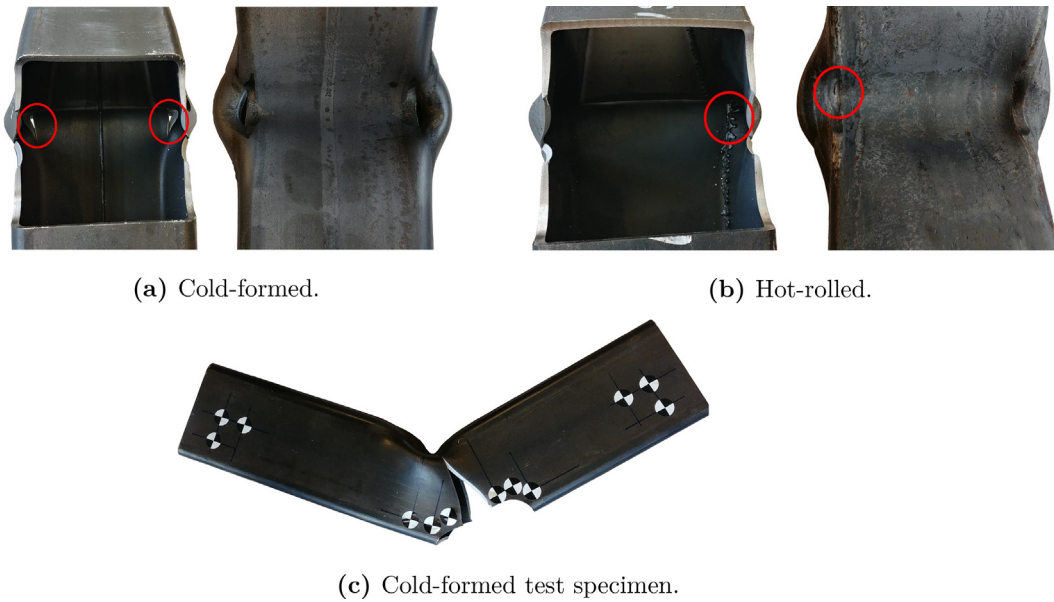
(a) Cold-formed.

(b) Hot-rolled.

(c) Cold-formed test specimen.

Fig. 15. Cracks observed in the dynamic test specimens.

5.2. Numerical simulations

The numerical models of the quasi-static simulations were repurposed for the dynamic simulations, with some minor modifications: time-scaling was removed, the actuator was assigned an initial velocity of 4.1 m/s and a mass of 1470.7 kg, and the diameter of the supports and actuator was reduced to 50 mm in order to match the new experimental test conditions. Further, a modified Johnson-Cook strain-rate sensitivity factor was included in the material model. The factor expands on the equation of the equivalent stress, which now reads

$$\sigma_{\text{eq}} = (\sigma_0 + R)\left(1 + \frac{\dot{p}}{\dot{p}_0}\right)^C \tag{8}$$

under yielding, where C is a material parameter, $\dot{p}$ is the equivalent plastic strain rate and $\dot{p}_0$ is a user-defined reference strain rate [38]. Note that the yield function f defined in Eq. (1) is now strictly positive at yielding. The strain-rate parameter C was set to 0.01 and the reference strain rate was set to $\dot{p}_0 = 0.0005$ s^{-1} [6]. These values from the literature were preferred over the moderate strain-rate data from the material tests presented here. Analysis of the strain rates from the simulations at the notch and below the impactor revealed values up to 120 s^{-1} with an average strain rate around 20 s^{-1}. This supports the choice of a customary value for the strain rate sensitivity instead of extrapolating from the tensile tests, where the strain rates only reached 0.1 s^{-1}.

The finite element simulations and the filtered results of the experimental tests are displayed in Fig. 14d to f. In line with the quasi-static model, the numerical simulations were not able to capture the same peak force as in the experimental tests. Furthermore, the ductility is somewhat overestimated in the simulations with the hot-rolled and off-shore steel. The displacement at failure in the cold-formed steel simulation seems to provide a good fit. However, the simulation did not capture the previously mentioned fractures in the top flange.

6. Discussion

One of the main objectives in the original paper by Costas et al. [18] was to reduce the mesh dependency of the failure criterion. The previously obtained test results and the numerical models of the quasi-static three-point bending tests were used for a mesh sensitivity analysis. Three mesh sizes which corresponded to element length-to-thickness ratios of one, two and three for the different steel types were employed in numerical simulations. The same numerical models as presented earlier were used. A comparison of the strain fields in the experimental and numerical results is also presented.

6.1. Strain fields

The black and white speckle pattern applied to the quasi-static test specimens was used to perform strain field analysis in eCorr. The same mesh as used for the simulations was imported from Abaqus to eCorr and placed around the notch. This was done in order to facilitate a direct comparison of strain fields in tests and simulations. An element length-to-thickness ratio of one was applied. The logarithmic strains in the axial direction of the specimens (ε_{11}) were plotted as color maps, see Fig. 16. Additionally, the location and value of the maximum strains are displayed. The strains were gathered at displacements right before failure in both the experimental tests and the numerical models.

A relevant point when comparing the strain fields is that DIC gathered surface strains of the steel sections, while the strains from Abaqus are obtained from shell elements. This limits the accuracy of the comparison, especially under strain localisation. As a general observation, the numerical simulations using shell elements did not capture the experimental localised strain fields around the notch. This is the case for all three steel types. The maximal strains in Abaqus were vastly underestimated. The determining factor in this case is the mesh size, which was limited to an element length-to-thickness ratio of 1. Apart from this, the overall form of the color-maps appears to represent the logarithmic strains in a good manner.

6.2. Impact of regularisation on mesh dependency

The stress-triaxiality ratio, defined as the hydrostatic stress divided by the equivalent von Mises stress, is an important measure in ductile fracture [15]. To check whether the stress state changed in the simulations when the aspect ratio was increased, the stress triaxiality was compared for the three steel materials. The stress triaxiality was acquired from Abaqus right before failure in the elements around the
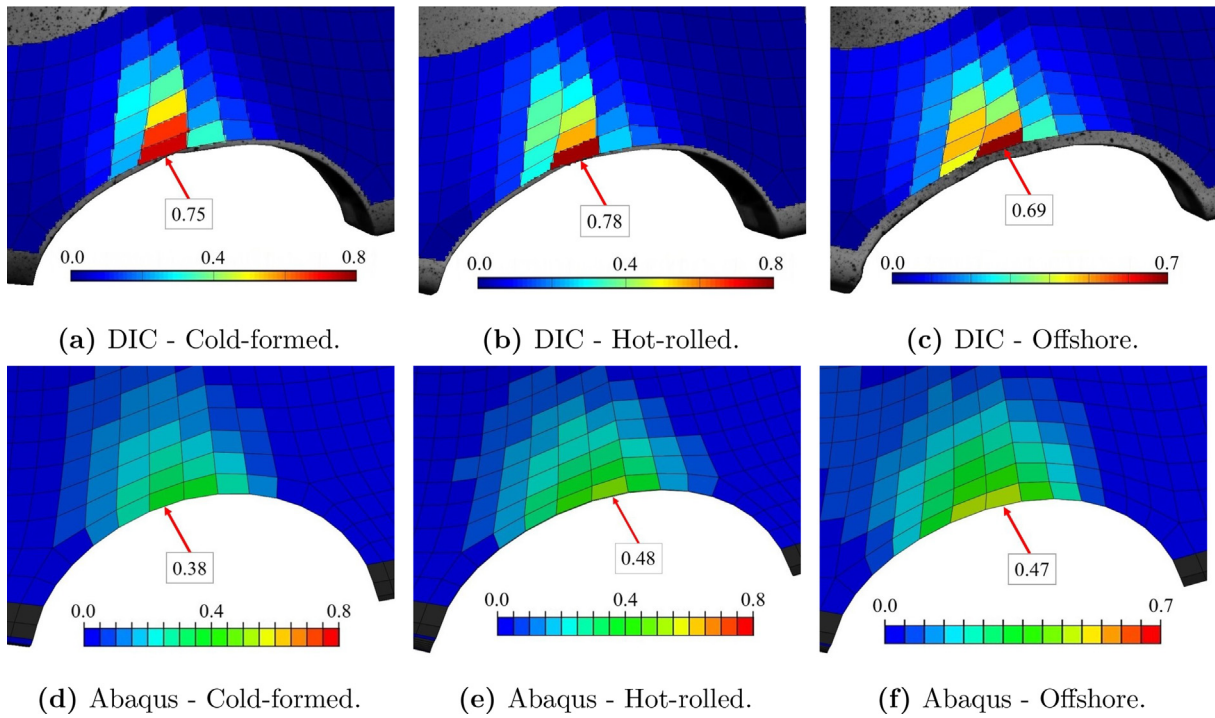
(a) DIC - Cold-formed.

(b) DIC - Hot-rolled.

(c) DIC - Offshore.

(d) Abaqus - Cold-formed.

(e) Abaqus - Hot-rolled.

(f) Abaqus - Offshore.

Fig. 16. Strain fields of axial logarithmic strains (ε_{11}) just before failure, which were obtained from eCorr and Abaqus for all three steel types. Maximal logarithmic strains are also displayed.

notch for the three mesh sizes. These were plotted against angles ranging from 0 to π in the notch. The location of the initiation of fracture was also plotted, see Fig. 17. It was observed that the stress triaxiality was consistently captured for all three steels, even when challenged by coarser mesh sizes.

In an effort to further validate the reduced mesh dependency of the regularisation model, three different failure modelling strategies were applied to the numerical models for the three steel types: (1) the TTR scheme as it was described earlier, (2) the Cockcroft-Latham fracture criterion with the failure parameter calibrated using a length-to-thickness ratio of one and DIC as described in Subsection 3.2, $W_C = W_C^s$, and (3) the Cockcroft-Latham fracture criterion with the failure parameter calibrated with small solid elements, $W_C = W_C^b$, see Subsection 3.2. The values of W_C^s and W_C^b provided in Table 4 were still employed. The simulations were run with three different mesh sizes. The results of the simulations are presented in Fig. 18. The displacement at failure

in the numerical simulations was defined as the first displacement where an element was eroded in the notch in Abaqus. It is apparent from Fig. 18a to c that the mesh sensitivity is reduced when using the TTR model. All three steel types were simulated with an element size corresponding to an aspect ratio of one. Failure was never reached in any of the elements when $W_C = W_C^b$, which can be observed in Fig. 18d. Therefore failure was vastly overestimated with this failure modelling strategy.

6.3. Outlook

The context for the material model and failure criterion adopted in this study is large-scale modelling of steel structures. The usual requirement for civil engineering purposes is to design structures according to a code, e.g. EN1993-1-1 [27], which gives guidelines for safe designs in the ultimate limit state. For most structures this is sufficient, perhaps
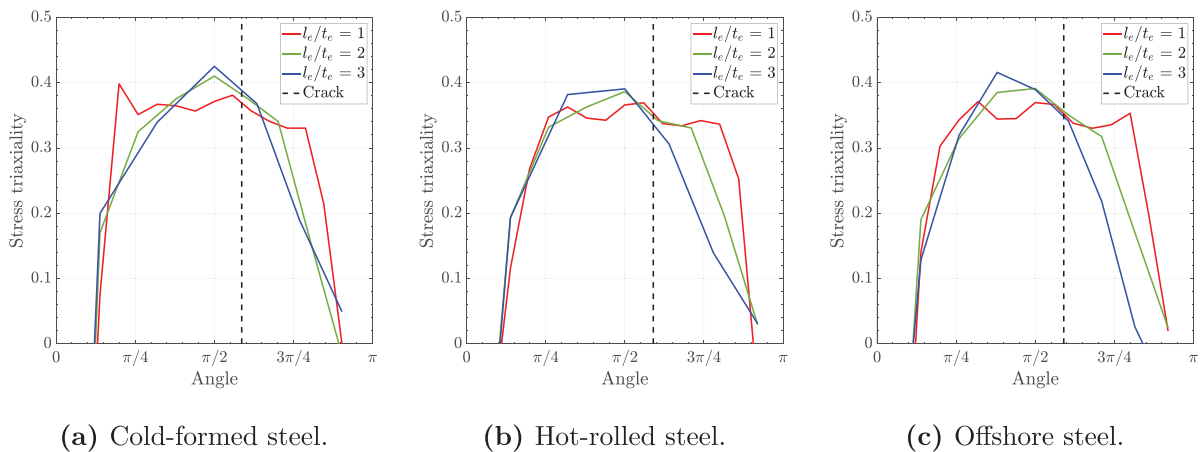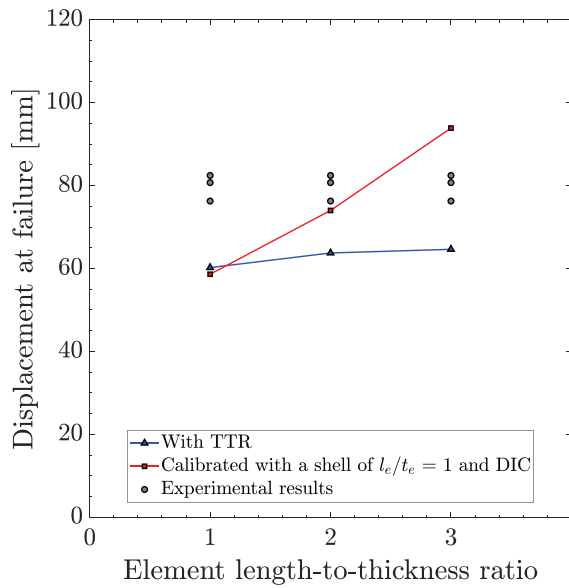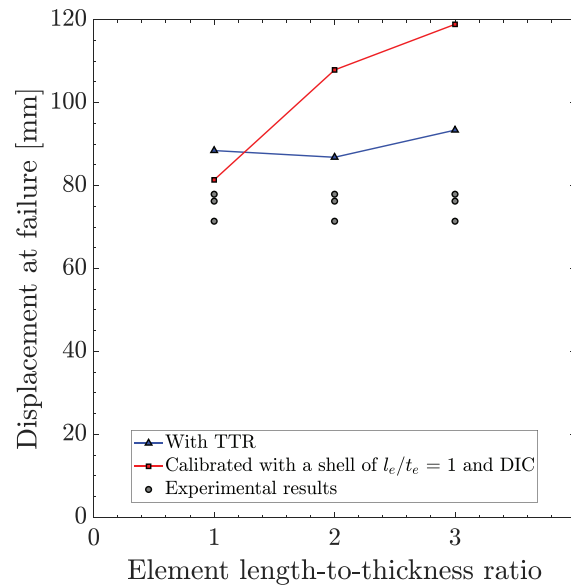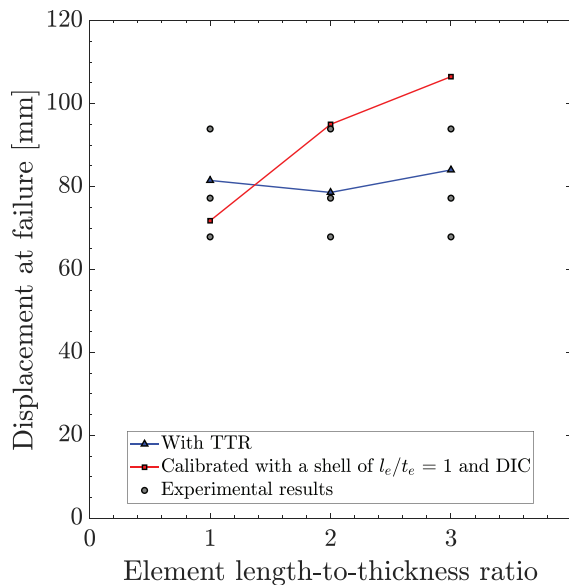

(a) Cold-formed steel.

(b) Hot-rolled steel.

(c) Offshore steel.

Fig. 17. Plots of stress triaxiality at elements around the notch in Abaqus simulations with different length-to-thickness ratios. The dashed line indicates the failure location.
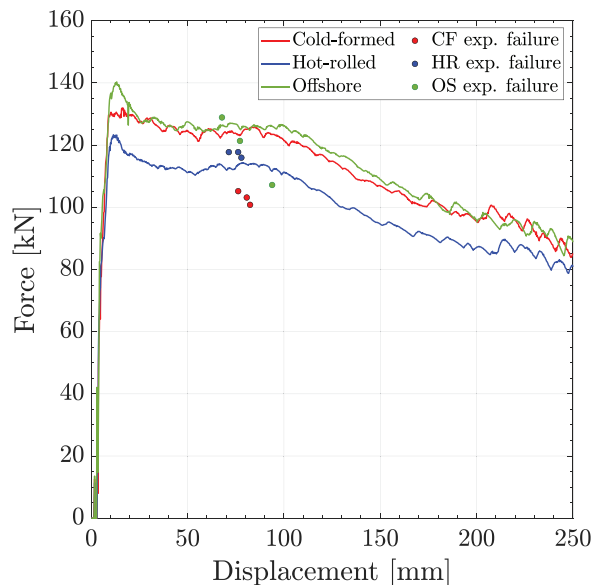
(a) Cold-formed steel.

(b) Hot-rolled steel.

(c) Offshore steel.

(d) W_C^b failure parameter.

Fig. 18. Displacement at failure with different approaches (a) (b) (c). Force-displacement curves of the three steel types with W_C^b as the only failure parameter and failure points from the experimental tests (d).

augmented with linear FE simulations for stress check, or nonlinear FE simulations to evaluate the extent of plastic zones.

However, there are situations where prediction of ductile failure in thin-walled steel members under bending and membrane loading may be of importance. Typical cases are e.g. ship impact, investigations of accidents, or design of energy absorbing structures. In such applications the modelling approach presented herein can give valuable insight at a small cost, as reasonable results are achieved with shell elements and standard modelling tools.

7. Conclusions

This experimental and numerical study investigated the mechanical behaviour of three different types of S355 square hollow sections under large deformations and failure. The through-thickness damage regularisation scheme proposed by Costas et al. [18] was benchmarked by running numerical simulations of the three steel types. The following main conclusions are drawn:

- The uniaxial tensile tests showed that there were notable differences in the material behaviour between the steel types. The offshore steel exhibited somewhat higher ductility than the hot-rolled and cold-formed steel. The cold-formed steel lacked a yield plateau and had the highest initial yield stress followed by the offshore steel. When performing three-point bending tests, the cold-formed steel experienced cracks in the top corners due to reduced ductility as a result of work-hardening during production.

- Numerical simulations of the notched component, applying the calibrated material models and a damage regularisation model, were able to capture the material behaviour and failure in the three steel types at both quasi-static and dynamic test conditions. Even with the limitations of the element discretisation caused by the thickness of the cross-section, the numerical model was able to predict failure using shells.

- Strain field mapping of the experimental and numerical test results showed that the numerical model captured the overall form of the strain distribution around the notch. Despite this, the numerical model underestimated the maximal strains.

- An evaluation of three different failure modelling strategies showed that the regularisation scheme reduced mesh dependency.

- The constitutive model and damage criterion applied herein may serve as useful tools when analysing failure in steel structures with shell elements.

Author statement

Håkon Johannessen: Carried out: Experimental tests, numerical simulations, treatment of data, preparation of manuscript

Oddvar H Johannessen: Carried out: Experimental tests, numerical simulations, treatment of data, preparation of manuscript

Miguel Costas: Advices on component tests. Contributed to numerical simulations and treatment of data. Revise of manuscript

Arild H Clausen: Contributed on component tests. Advices on experimental tests in general, numerical simulations and treatment of data. Revise of manuscript.

Johan K Sønstabø: Initiation of study. Advices on experimental and numerical study. Revise of manuscript.

Declaration of Competing Interest

The authors declare that they do not have any competing financial interests or personal relationships that could have appeared to influence the work reported in this article.

Acknowledgements

References

[1] L. Gardner, N. Saari, F. Wang, Comparative experimental study of hot-rolled and cold-formed rectangular hollow sections, Thin-Walled Struct. 48 (7) (2010) 495–507.

[2] Y.J. Guo, A.Z. Zhu, Y.L. Pi, F. Tin-Loi, Experimental study on compressive strengths of thick-walled cold-formed sections, J. Constr. Steel Res. 63 (5) (2007) 718–723.

[3] W.M. Quach, B. Young, Material properties of cold-formed and hot-finished elliptical hollow sections, Adv. Struct. Eng. 18 (7) (2015) 1101–1114.

[4] M. Sun, J.A. Packer, Direct-formed and continuous-formed rectangular hollow sections — comparison of static properties, J. Constr. Steel Res. 92 (2014) 67–78.

[5] M. Sun, J.A. Packer, High strain rate behaviour of cold-formed rectangular hollow sections, Eng. Struct. 62–63 (2014) 181–192.

[6] V. Aune, G. Valsamos, F. Casadei, M. Langseth, T. Børvik, On the dynamic response of blast-loaded steel plates with and without pre-formed holes, Int. J. Impact Eng. 108 (2017) 27–46.

[7] E.L. Grimsmo, A.H. Clausen, A. Aalberg, M. Langseth, A numerical study of beam-to-column joints subjected to impact, Eng. Struct. 120 (C) (2016) 103–115.

[8] D. Forni, B. Chiaia, E. Cadoni, Strain rate behaviour in tension of s355 steel: base for progressivecollapse analysis, Eng. Struct. 119 (2016) 164–173.

[9] Y. Yamada, H. Endo, P. Pedersen, Effect of buffer bow structure in ship-ship collision, Int. J. Offshore Polar Eng. 18 (2) (2008) 133–141.

[10] P. Hogström, J.W. Ringsberg, E. Johnson, An experimental and numerical study of the effects of length scale and strain state on the necking and fracture behaviours in sheet metals, Int. J. Impact Eng. 36 (10−11) (2009) 1194–1203.

[11] J.D. Bressan, J.A. Williams, The use of a shear instability criterion to predict local necking in sheet metal deformation, Int. J. Mech. Sci. 25 (3) (1983) 155–168.

[12] R. Hill, On discontinuous plastic states, with special reference to localized necking in thin sheets, J. Mech. Phys. Solids 1 (1) (1952) 19–30.

[13] H.S. Alsos, O.S. Hopperstad, R. Toernqvist, J. Amdahl, Analytical and numerical analysis of sheet metal instability using a stress based criterion, Int. J. Solids Struct. 45 (7–8) (2008) 2042–2055.

[14] M. Kõrgesaar, H. Remes, J. Romanoff, Size dependent response of large shell elements under in-plane tensile loading, Int. J. Solids Struct. 51 (21−22) (2014) 3752–3761.

[15] M. Kõrgesaar, J. Romanoff, Influence of mesh size, stress triaxiality and damage induced softening on ductile fracture of large-scale shell structures, Mar. Struct. 38 (2014) 1–17.

[16] C.L. Walters, Framework for adjusting for both stress triaxiality and mesh size effect for failure of metals in shell structures, Int. J. Crashworthiness 19 (1) (2014) 1–12.

[17] R.G. Andersen, J.G. Londono, P.B. Woelke, K.L. Nielsen, Fundamental differences between plane strain bending and far-field plane strain tension in ductile plate failure, J. Mech. Phys. Solids 141 (2020) 103960.

[18] M. Costas, D. Morin, O.S. Hopperstad, T. Børvik, M. Langseth, A through-thickness damage regularisation scheme for shell elements subjected to severe bending and membrane deformations, J. Mech. Phys. Solids 123 (2019) 190–206.

[19] CEN, NS-EN 10219-2:2019, Cold formed welded structural hollow sections of non-alloy and fine grain steels - Part 2: Tolerances, dimensions and sectional properties, European Standard, 2019.

[20] CEN, NS-EN 10210-2:2019, Hot finished structural hollow sections of non-alloy and fine grain steels - Part 2: Tolerances, dimensions and sectional properties, European Standard, 2019.

[21] CEN, NS-EN 10219-1:2006, Cold formed welded structural hollow sections of non-alloy and fine grain steels - Part 1: Technical delivery conditions, European Standard, 2006.

[22] CEN, NS-EN 10210-1:2006, Hot finished structural hollow sections of non-alloy and fine grain steels - Part 1: Technical delivery conditions, European Standard, 2006.

[23] CEN, NS-EN 10225-3:2019, Weldable structural steels for fixed offshore structures - Technical delivery conditions - Part 3: Hot finished hollow sections, European Standard, 2019.

[24] L. Tong, G. Hou, Y. Chen, F. Zhou, K. Shen, A. Yang, Experimental investigation on longitudinal residual stresses for cold-formed thick-walled square hollow sections, J. Constr. Steel Res. 73 (2012) 105–116.

[25] E. Fagerholt, T. Børvik, O.S. Hopperstad, Measuring discontinuous displacement fields in cracked specimens using digital image correlation with mesh adaptation and crack-path optimization, Opt. Lasers Eng. 51 (3) (2013) 299–310.

[26] User manual - eCorr - Digital Image Correlation Tool, https://www.ntnu.edu/kt/ecorr Accessed: 2020-06-09.

[27] CEN, NS-EN 1993-1-1:2005/A1, Eurocode 3: Design of steel structures - Part 1-1: General rules and rules for buildings, European Standard, 2014.

[28] LS-OPT User's Manual, Version 6.0. , Livermore Software Technology Corporation, Livermore, California, 2019.

[29] ABAQUS, 6.14 Documentation, Dassault Systèmes, Providence Road, Rhode Island, 2014.

[30] M.G. Cockcroft, D.J. Latham, Ductility and the workability of metals, J. Inst. Met. 96 (1) (1968) 33–39.

[31] D. Morin, B.L. Kaarstad, B. Skajaa, O.S. Hopperstad, M. Langseth, Testing and modelling of stiffened aluminium panels subjected to quasi-static and low-velocity impact loading, Int. J. Impact Eng. 110 (C) (2017) 97–111.

[32] A.G. Hanssen, T. Auestad, T. Tryland, M. Langseth, The kicking machine: a device for impact testing of structural components, Int. J. Crashworthiness 8 (4) (2003) 385–392.

[33] O. Vestrum, M. Kristoffersen, M.A. Polanco-Loria, H. Ilstad, M. Langseth, T. Børvik, Quasi-static and dynamic indentation of offshore pipelines with and without multi-layer polymeric coating, Mar. Struct. 62 (2018) 60–76.

[34] G. Gruben, S. Sølvernes, T. Berstad, D. Morin, O.S. Hopperstad, M. Langseth, Low-velocity impact behaviour and failure of stiffened steel plates, Mar. Struct. 54 (2017) 73–91.

[35] M. Costas, D. Morin, M. Langseth, L. Romera, J. Díaz, Axial crushing of aluminum extrusions filled with PET foam and GFRP. An experimental investigation, Thin-Walled Struct. 99 (C) (2016) 45–57.

[36] J.K. Sønstabø, D. Morin, M. Langseth, Static and dynamic testing and modelling of aluminium joints with flow-drill screw connections, Int. J. Impact Eng. 115 (2018) 58–75.

[37] E.L. Grimsmo, A.H. Clausen, M. Langseth, A. Aalberg, An experimental study of static and dynamic behaviour of bolted end-plate joints of steel, Int. J. Impact Eng. 85 (C) (2015) 132–145.

[38] T. Børvik, O.S. Hopperstad, T. Berstad, M. Langseth, A computational model of viscoplasticity and ductile damage for impact and penetration, Eur. J. Mech. A Solids 20 (5) (2001) 685–712.